2000

# A Navier-Stokes analysis of the stall flutter characteristics of the Buffum cascade

Weber, Stefan; Platzer, Max F.

ASME

S. Weber, M.F. Platzer, "A Navier-Stokes analysis of the stall flutter characteristics of the Buffum cascade," Journal of Turbomachinery, v.122, (October 2000), pp.769-776
http://hdl.handle.net/10945/55673

# A Navier–Stokes Analysis of the Stall Flutter Characteristics of the Buffum Cascade

**Stefan Weber**
Post-Doctoral Research Associate,
Deutsche Forschungsgemeinschaft,

**Max F. Platzer**
Professor,
Fellow ASME

Department of Aeronautics and Astronautics,
Naval Postgraduate School,
Monterey, CA 93943-5000

*Numerical stall flutter prediction methods are much needed, as modern jet engines require blade designs close to the stability boundaries of the performance map. A Quasi-3D Navier–Stokes code is used to analyze the flow over the oscillating cascade designed and manufactured by Pratt & Whitney, and studied at the NASA Glenn Research Center by Buffum et al. The numerical method solves for the governing equations with a fully implicit time-marching technique in a single passage by making use of a direct-store, periodic boundary condition. For turbulence modeling, the Baldwin–Lomax model is used. To account for transition, the criterion to predict the onset location suggested by Baldwin and Lomax is incorporated. Buffum et al. investigated two incidence cases for three different Mach numbers. The low-incidence case at a Mach number of 0.5 exhibited the formation of small separation bubbles at reduced oscillation frequencies of 0.8 and 1.2. For this case the present approach yielded good agreement with the steady and oscillatory measurements. At high incidence at the same Mach number of 0.5 the measured steady-state pressure distribution and the separation bubble on the upper surface was also found in good agreement with the experiment. But computations for oscillations at high incidence failed to predict the negative damping contribution caused by the leading edge separation.* [S0889-504X(00)01304-0]

## Introduction

A review of aeroelastic prediction methods for axial-flow turbomachinery [1] showed that the commonly used unsteady flow models were limited to two-dimensional linearized methods. During the past twelve years, tremendous advances in CFD have made it possible to replace some of these models by nonlinear three-dimensional flow models. However, the simulation of strong viscous flow effects is still fraught with many uncertainties, making it difficult to predict some important aeroelastic phenomena. One of these phenomena is stall flutter, where the currently used empirical correlations for the stall flutter boundary prediction of compressor and fan blades have yet to be replaced by ''rational'' computational methods based on the solution of the Navier–Stokes equations. These uncertainties are caused by the well-recognized difficulties to model laminar-to-turbulent flow transition and turbulent flow in the presence of strong flow oscillations. Furthermore, it is likely that stall flutter cannot be modeled by purely two-dimensional methods because separated flows tend to be three-dimensional. This situation is complicated even further for the case of high subsonic/transonic stall flutter due to the formation of shock waves.

In this situation the computational fluid dynamicist has no choice but to proceed to increasingly more demanding flow modeling and to evaluate the validity of the model against well-controlled experiments. Most investigators are agreed that the modeling has to be based on the Navier–Stokes equations. However, great savings in CPU times can be achieved if the flow is decomposed into a steady nonlinear flow upon which small harmonic perturbations are superimposed. The most recent example for this type of approach was presented by Clark and Hall [2] following the work of Hall and Crawley [3], Kahl and Klose [4], and Montgomery and Verdon [5]. On the other hand, time linearization imposes limits on the oscillation amplitudes and hence it is prudent to evaluate time-linearized results against solutions of the nonlinearized unsteady Navier–Stokes equations. Furthermore, recent steady and dynamic stall computations for single airfoils have yielded markedly improved agreement with measured hysteresis loops if the Baldwin and Lomax [6] algebraic turbulence model was replaced by the one-equation Baldwin and Barth [7] and Spalart and Allmaras [8] models and the laminar-to-turbulent transition onset and length was incorporated into computations, as shown by Ekaterinaris and Platzer [9], Sanz and Platzer [10], Weber and Platzer [11], Weber et al. [12], and Eulitz [13].

The approach presented in this paper is based on the reasoning given above. Although three-dimensional flutter computations are presently being developed, for example by Bakhle [14] and Chew et al. [15], we believe that such an approach is still premature for the analysis of stall flutter. Therefore, the present analysis is based on the Quasi-3D Navier–Stokes equations without any further linearization assumptions. Such an approach was also adopted by He [16], Eguchi and Wiedermann [17], Abhari and Giles [18], Grüber and Carstens [19], Weber et al. [20,21], Kato et al. [22], Tuncer et al. [23], Carstens and Schmitt [24], Fourmaux [25], and Lin and Murthy [26]. The turbulence modeling still relies on the simple algebraic Baldwin–Lomax model, but the transition onset criterion introduced by Baldwin–Lomax is incorporated. The results are evaluated by comparison with the oscillating cascade measurements of Buffum et al. [27] which appear to be the most reliable data for such a comparison at the present time.

## Mathematical Model

The present algorithm solves the nondimensinalized time-dependent Quasi-3D Navier–Stokes equations. The equations are derived for an $m$, $\varphi$-coordinate system with $m$ in axial and $\varphi$ in circumferential direction. It represents S1-stream surfaces of revolution at a radius $r$ with a variable stream surface thickness $B$ to account for three-dimensional flow effects. Following Benetschik [28], the Favre-averaged governing equations in strong conservation law-form transformed to curvilinear coordinates ($\xi$, $\eta$) can be given in a rotating frame of reference as follows:

$$\partial_t \hat{\mathbf{U}} + \partial_\xi \left( \hat{\mathbf{E}} - \frac{1}{\mathrm{Re}} \hat{\mathbf{E}}_v \right) + \partial_\eta \left( \hat{\mathbf{F}} - \frac{1}{\mathrm{Re}} \hat{\mathbf{F}}_v \right) = \hat{\mathbf{Q}} \qquad (1)$$

Contributed by the International Gas Turbine Institute and presented at the 45th International Gas Turbine and Aeroengine Congress and Exhibition, Munich, Germany, May 8–11, 2000. Manuscript received by the International Gas Turbine Institute February 2000. Paper No. 2000-GT-385. Review Chair: D. Ballal.

  

in which $J=\partial(m,\varphi)/\partial(\xi,\eta)$ is the Jacobian matrix of transformation, and where $\hat{\mathbf{U}}$ is the vector of conservative variables

$$\hat{\mathbf{U}}=JrB\begin{Bmatrix}\rho\\ \rho v_m\\ \rho r v_\varphi\\ \theta_{\mathrm{rot}}\end{Bmatrix}, \tag{2}$$

$\hat{\mathbf{E}}$ and $\hat{\mathbf{F}}$ are the Euler fluxes

$$\hat{\mathbf{E}}=JB\begin{Bmatrix}\rho W^\xi\\ \rho v_m W^\xi+rp\xi_m\\ \rho r v_\varphi W^\xi+rp\xi_\varphi\\ e_{\mathrm{rot}}W^\xi+pw^\xi\end{Bmatrix}, \tag{3}$$

$$\hat{\mathbf{F}}=JB\begin{Bmatrix}\rho W^\eta\\ \rho v_m W^\eta+rp\eta_m\\ \rho r v_\varphi W^\eta+rp\eta_\varphi\\ e_{\mathrm{rot}}W^\eta+pw^\eta\end{Bmatrix}, \tag{4}$$

and $\hat{\mathbf{E}}_v$ and $\hat{\mathbf{F}}_v$ the viscous fluxes

$$\hat{\mathbf{E}}_v=J\begin{Bmatrix}0\\ r\rho\tau_{mm}\xi_{mm}+\tau_{m\varphi}\xi_\varphi\\ r(r\rho\tau_{m\varphi}\xi_{mm}+\tau_{\varphi\varphi}\xi_\varphi)\\ rE_{ev}\xi_m+F_{ev}\xi_\varphi\end{Bmatrix}, \tag{5}$$

$$\hat{\mathbf{F}}_v=J\begin{Bmatrix}0\\ r\rho\tau_{mm}\eta_{mm}+\tau_{m\varphi}\eta_\varphi\\ r(r\rho\tau_{m\varphi}\eta_{mm}+\tau_{\varphi\varphi}\eta_\varphi)\\ rE_{ev}\eta_m+F_{ev}\eta_\varphi\end{Bmatrix}, \tag{6}$$

where

$$E_{ev}=w_m\tau_{mm}+w_\varphi\tau_{m\varphi}+q_m, \tag{7}$$

$$F_{ev}=w_m\tau_{m\varphi}+w_\varphi\tau_{\varphi\varphi}+q_\varphi, \tag{8}$$

and the source vector $\hat{\mathbf{Q}}$ due to the coordinate transformation for the S1-system

$$\hat{\mathbf{Q}}_v=JrB\begin{Bmatrix}0\\ \rho v_\varphi^2\dfrac{1}{r}\dfrac{\partial r}{\partial m}+\dfrac{p}{rB}\dfrac{\partial rB}{\partial m}\\ 0\\ 0\end{Bmatrix}. \tag{9}$$

The transformed components of the heat flux $q$ and the stress tensor $\tau$ are given in more detail in Weber et al. [20]. In these equations $\rho$ denotes the density and $p$ the pressure. The absolute and relative velocity components are $v_m, v_\varphi$, and $w_m, w_\varphi$, respectively. The contravariant velocities $W^\xi$ and $W^\eta$ are given by:

$$W^\xi=r\xi_m(w_m-c_{\xi m})+\xi_\varphi(w_\varphi-c_{\xi\varphi}) \tag{10}$$

and

$$W^\eta=r\eta_m(w_m-c_{\eta m})+\eta_\varphi(w_\varphi-c_{\eta\varphi}) \tag{11}$$

with the components of the contravariant cell face velocities $c^\xi, c^\eta$ which have to be introduced due to the time-dependent deformation of the grid. The volume specific total energy $e_{\mathrm{rot}}$ and the rothalpy $H_{\mathrm{rot}}$ assuming perfect gas are defined as:

$$e_{\mathrm{rot}}=\frac{p}{\kappa-1}+\frac{\rho}{2}(v_m^2+v_\varphi^2)-\Omega r\rho v_\varphi \tag{12}$$

and

$$H_{\mathrm{rot}}=\frac{e_{\mathrm{rot}}+p}{\rho} \tag{13}$$

with $\kappa$ the ratio of the specific heats, and $\Omega$ in case of a rotor flow as the angular velocity. To model the turbulent stresses, a turbulent eddy viscosity is computed following the turbulence model of Baldwin and Lomax [6]. The laminar viscosity is predicted by Sutherland's law. The onset of laminar/turbulent transition is found with the criterion suggested by Baldwin and Lomax [6] using $C_{mutm}$ of 14. Furthermore, an effective thermal transport coefficient is introduced, using a laminar and a turbulent Prandtl number.

Equation (1) is nondimensionalized referring to the free-stream total density, the free-stream total velocity of sound, the free-stream total viscosity, and the chord length.

## Numerical Method

A finite volume technique is applied for the numerical solution of Eq. (1), which is discretized in a node-centered form. Central and antisymmetric differences are used to compute the viscous fluxes. The inviscid fluxes are computed with an upwind FDS scheme by Roe [29]. At each volume cell face it solves for an approximative Riemann problem by computing a numerical flux function. For example in the $\xi$ direction, the definition of the flux function for a cell face located at $(i+1/2,j)$ is:

$$\hat{\mathbf{E}}(\hat{\mathbf{U}})_{i+1/2,j}=\frac{1}{2}[\hat{\mathbf{E}}(\hat{\mathbf{U}}_L)_{i+1/2}+\hat{\mathbf{E}}(\hat{\mathbf{U}}_R)_{i+1/2} -(\hat{\mathbf{R}}^\xi|\hat{\mathbf{\Lambda}}^\xi|\hat{\mathbf{L}}^\xi(\hat{\mathbf{U}}_R-\hat{\mathbf{U}}_L))_{i+1/2}] \tag{14}$$

with the initial state vectors $\hat{\mathbf{U}}_L$ at the left and $\hat{\mathbf{U}}_R$ at the right side of the cell face, $\hat{\mathbf{L}}^\xi$ the left and $\hat{\mathbf{R}}^\xi$ the right matrices of the left and the right eigenvectors, respectively and $\hat{\mathbf{\Lambda}}^\xi$ the diagonal matrix of eigenvalues with respect to $\hat{\mathbf{E}}$. The components of the matrices are obtained using the Roe average.

With Eq. (14), a characteristic wave decomposition is achieved, resulting in two acoustic waves, one shear, and one entropy wave. Herein the eigenvalues describe the characteristic speed and the direction of the waves. Consistent with the characteristic compatibility relations, the change of the characteristic variable across the cell face can be computed due to the particular eigenvalue formulation.

To assure a minimum amount of artificial viscosity in the whole computational domain, a method suggested by Harten [30] is implemented, as well as a correction of the eigenvalues to overcome a nonphysical negative entropy change across expansion fans. The spatial discretization of the inviscid fluxes is extended to third-order accuracy by applying the MUSCL technique [31] together with the TVD scheme by Harten [30] and the van Albada limiter function to avoid stability problems.

The fully implicit time-integration of Eq. (1) is performed second-order accurate in time following the scheme of Rai and Chakravarthy [32]. Time accuracy is improved by using Newton subiterations to minimize linearization errors at each time step while the system of equations itself is solved iteratively by a Gauss–Seidel relaxation method. For unsteady computations best performance in terms of accuracy and convergence was found by using three Newton subiterations at each time step.

**Boundary Conditions and Unsteady Grid Generation.** The numerical treatment of the far field boundary conditions follows a method of characteristics proposed by Chakravarthy [33]. For the up- and downstream boundaries, the number of physical boundary conditions depends on the number of characteristics entering the computational domain neglecting all viscous terms. At the inflow boundary the total pressure, the total temperature, and the inflow angle are imposed. At the outflow boundary only the exit pressure is prescribed. For viscous flows Stokes' nonslip condition is applied on the surface of the blade, assuming an adiabatic wall and a vanishing normal pressure gradient. The assumption of a zero normal pressure gradient for unsteady flows is still correct if the reduced frequency of the blade oscillation is small.

At the periodic boundary use is made of the direct store method introduced by Erdos et al. [34]. This boundary condition allows the simulation of harmonically oscillating blades for any interblade phase angle with only one passage. Convergence is achieved if the difference between the flow quantities compared with the flow quantities of the previous cycle are below a certain limit. To avoid large storage requirements, the flow variables at the periodic boundaries are not stored at each time step, making use of a technique introduced by Peitsch et al. [35].

The simulation of the blade motion requires an unsteady regeneration of the C- or O-type grid. Therefore, the grid is divided into three zones. The first zone includes the blade surface and the grid lines inside the boundary layer preserving the orthogonality of the grid on the surface. This zone moves as a solid body according to the chosen mode of oscillation. Wrapped around the first zone is the second zone, which is surrounded by a stationary nondeforming third zone. The second zone is deformed at each time step and the grid is regenerated by solving the Laplace equation. Experience shows that it is not necessary to run the grid regeneration at each time step. Instead, it is sufficient to use a linear interpolation between newly regenerated grids. The third zone is kept fixed to save the orthogonality of the grid at the outer boundaries.

The Navier–Stokes code has been tested extensively for a variety of steady and unsteady subsonic and transonic test cases, such as [20,21,28].

## Computational Results and Discussion

Computations were performed to investigate the flutter characteristics of the Buffum cascade. This cascade was developed to improve the understanding of the unsteady flow phenomena which cause stall flutter. The measurements were taken in the wind tunnel of the NASA Glenn Research Center, where this linear nine-blade cascade was installed. A series of steady and oscillatory measurements were taken for free-stream Mach numbers of 0.2, 0.5, and 0.8 at low and high incidence. In the experiment all blades were executing a harmonic pitching motion around the midchord point with an amplitude $\hat{\alpha}$ of 1.2 deg at an interblade phase angle $\Phi$ of 180 deg. The reduced frequency $k=2\pi fc/U_\infty$ was varied between 0.4 and 1.2. The stagger angle $\gamma$ of the low-aspect-ratio fan blade tip section was 60 deg, the chord length $c$ was 0.0889 m, and the solidity $c/s$ was 1.52.

In this paper we analyze only the steady and oscillatory data for a free-stream Mach number of 0.5 and a Reynolds number Re of $0.9\times10^6$. The corresponding experimental results as well as the details of the test facility were discussed and given in detail by Buffum et al. [27].

All steady-state and unsteady computations for the Buffum cascade were performed on an O-type $241\times61$ point Navier–Stokes grid. Several grids were tested and the initial wall spacing decreased until the solution became independent of the grid for $y^+<1.5$. The grid is shown in Fig. 1, including a magnification of the leading edge (top left) and the trailing edge (bottom right).

**Steady-State Low-Incidence Flow.** Before running an unsteady computation, a steady-state solution was computed. In Buffum et al. [27], the in-flow angle $\alpha$ corresponding to low incidence was given to be 60 deg at a pressure ratio $p_{\text{exit}}/p_\infty$ of 0.93. In order to obtain good agreement with the experimental data, the pressure ratio for the numerical simulation had to be changed to 0.936, resulting in an averaged inflow angle of 61.1 deg. The computed data were compared with the measured chordwise pressure coefficient distributions with a definition of the steady pressure coefficient as follows:

$$Cp\left(\frac{x}{c}\right)=\frac{p\left(\frac{x}{c}\right)-p_\infty}{\rho_\infty U_\infty^2}. \tag{15}$$

Two steady-state computations, one fully turbulent and one including transition, were performed. In Fig. 2 the predicted pressures are seen to compare well with the experimental data.

Figure 2 also includes experimental data on the neighboring blades to indicate the degree of periodicity in the test cascade. The difference between the development of the boundary layer without and with transition is seen to be small. A re-laminarization was predicted at the trailing edge while the strongest influence of transition could be seen close to the leading edge. In Fig. 3 the pressure distribution at the leading edge is given in more detail. Both computations predicted the stagnation point slightly on the lower surface, reaching a $Cp$ of 0.5. Starting from the stagnation point, the flow was accelerated on both surfaces of the blade, as can be seen from the two suction peaks. The higher acceleration was

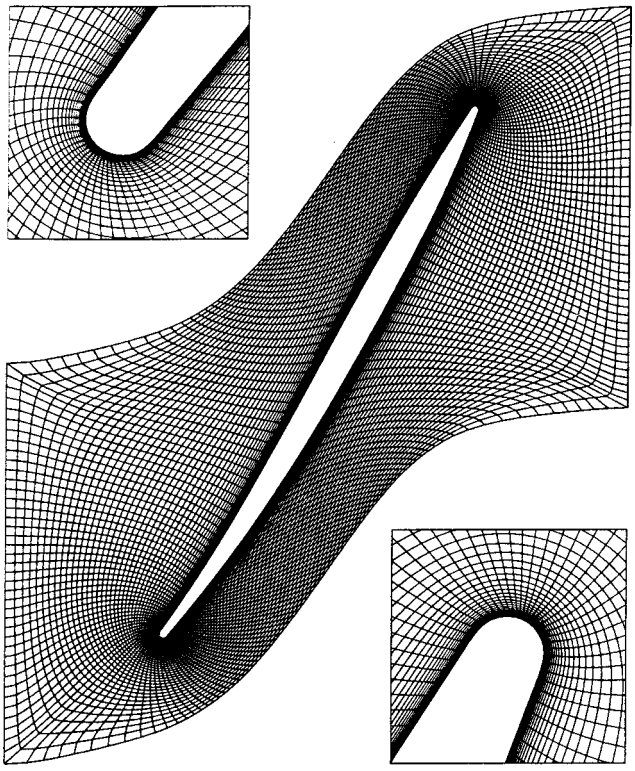

**Fig. 1 O-type 241×61 point grid for the Buffum cascade**

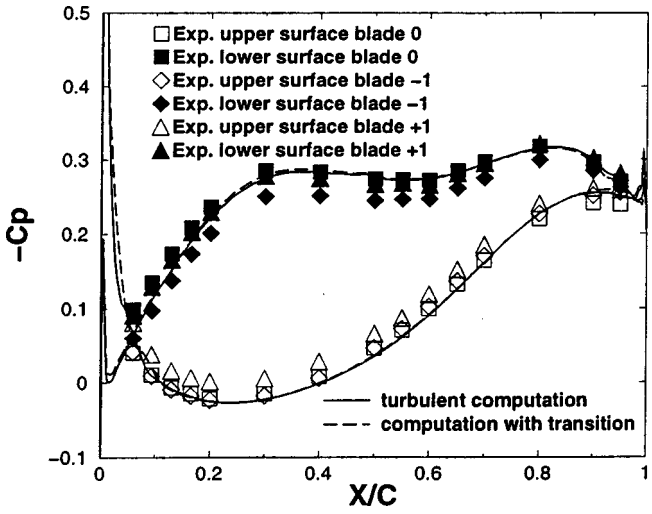


**Fig. 2 Steady-state pressure distribution, $M=0.5$, $\alpha=61.1$ deg, $\text{Re}=0.9\times10^6$**

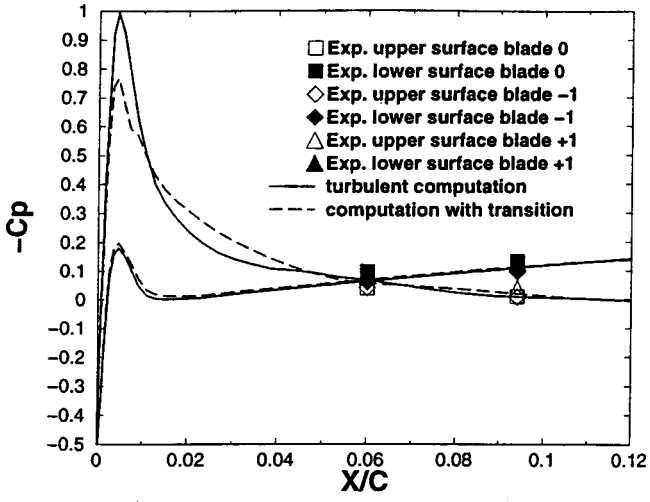


**Fig. 3 Steady-state pressure distribution at leading edge, $M=0.5$, $\alpha=61.1$ deg, $\mathrm{Re}=0.9\times10^6$**

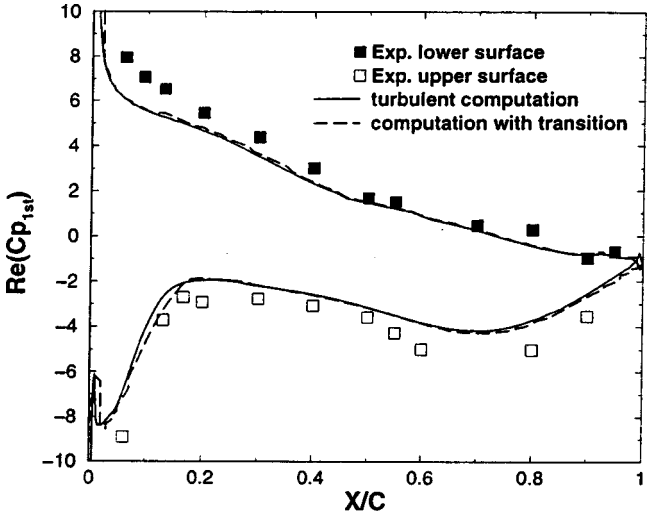


**Fig. 5 Real part of unsteady pressure distribution at low incidence, $k=1.2$, $\Phi=180$ deg, $M=0.5$, $\mathrm{Re}=0.9\times10^6$**

found on the upper surface, e.g., the fully turbulent flow prediction reached a $Cp$ of $-1$ (Fig. 3). The transition criterion of Baldwin–Lomax predicted a laminar region for 11 percent chord length on the lower surface. On the upper surface the turbulent flow started at 1 percent chord length. Furthermore, a separation bubble was found on the upper surface. The bubble length was approximately 5.5 percent of chord length independent of transition, while the bubble size was bigger for the computation, including transition. The predicted steady-state velocity vector distribution including transition is given in Fig. 4. One can see that the separation occurs on the upper surface of the blade at the point where the curvature of the blade surface changes sign.

**Flutter at Low Incidence.** At low incidence oscillatory measurements were taken for reduced frequencies of 0.4, 0.8, and 1.2. However, for $k=0.4$, the measured data have not been published because the passage-to-passage periodicity was too poor. For analysis of the unsteady data a first harmonic unsteady pressure coefficient is defined as follows:

$$Cp_{1st}\left(\frac{x}{c}\right)=\frac{p_{1st}\left(\frac{x}{c}\right)}{\hat{\alpha}\rho_\infty U_\infty^2}. \tag{16}$$

In Figs. 5 and 6 the real or in-phase part Re( ) and the imaginary or out-of-phase part Im( ) of the first harmonic unsteady pressure coefficient are compared with the experimental data for a reduced frequency of 1.2.

The real part is seen to agree well with the measured data. Again, the fully turbulent computation differed only slightly from the computation, including transition. The biggest difference was found on the upper surface of the blade between the leading edge and 16 percent chord length. Although the trend of the measured out-of-phase part of the unsteady pressure is predicted well, the quantitative agreement is worse than for the in-phase part. The influence of transition is again strongest on the upper surface between the leading edge and 16 percent chord length. Similar re-

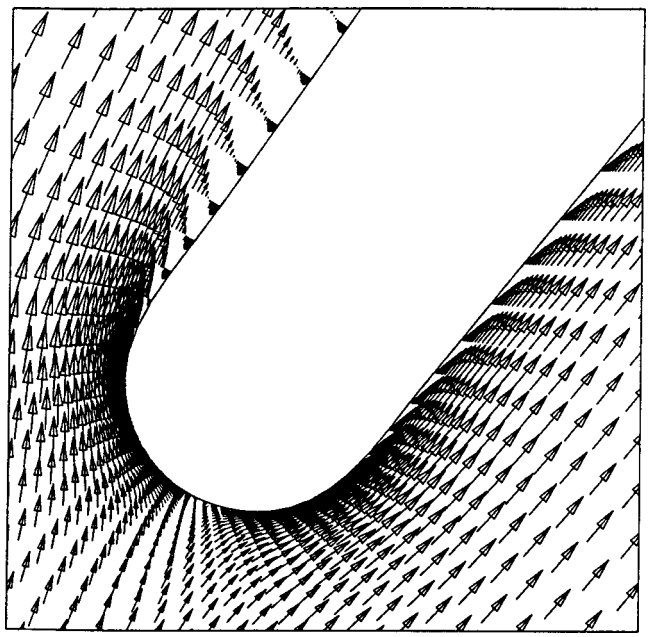

**Fig. 4 Steady-state velocity vectors at leading edge, $M=0.5$, $\alpha=61.1$ deg, $\mathrm{Re}=0.9\times10^6$**

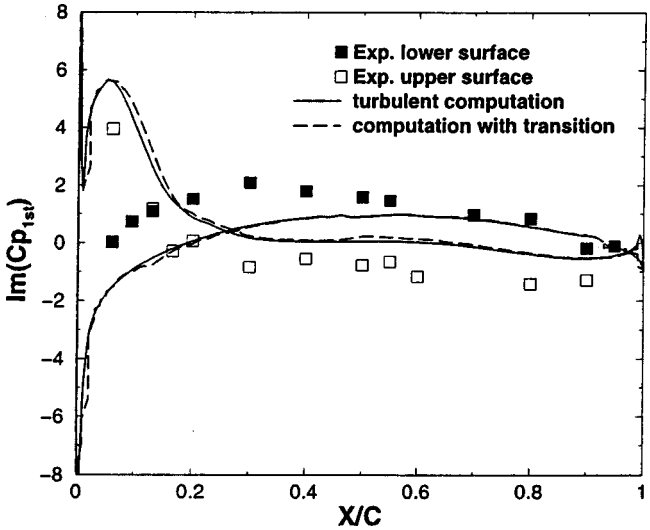


**Fig. 6 Imaginary part of unsteady pressure distribution at low incidence, $k=1.2$, $\Phi=180$ deg, $M=0.5$, $\mathrm{Re}=0.9\times10^6$**

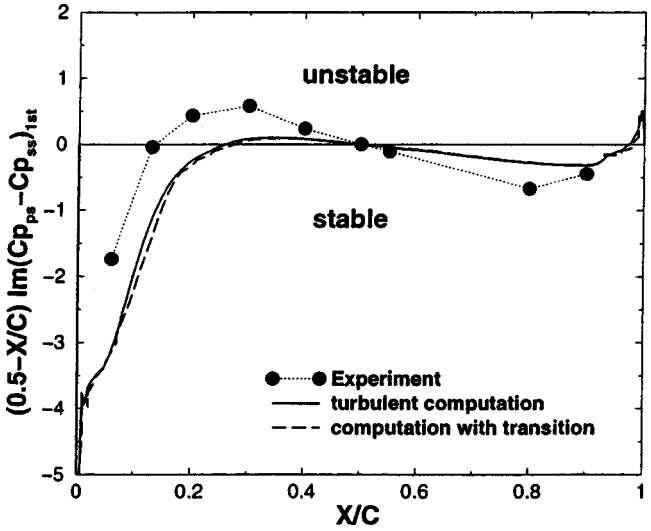


**Fig. 7 Local stability analysis at low incidence, $k=1.2$, $\Phi=180$ deg, $M=0.5$, $\mathrm{Re}=0.9\times10^6$**

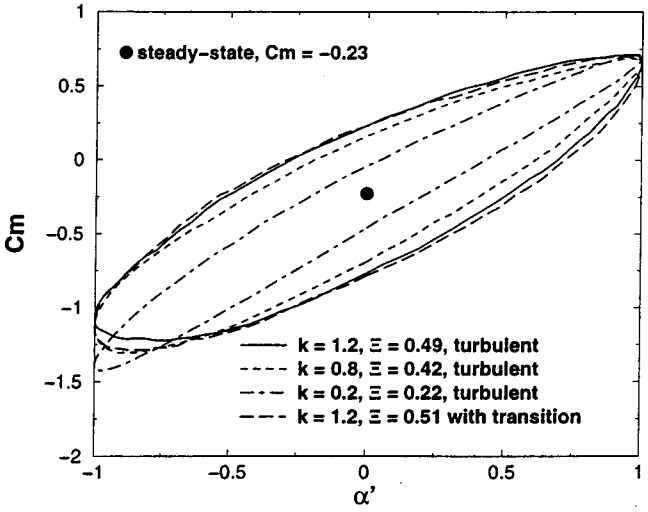


**Fig. 9 Predicted pitching moment coefficient at low incidence, $\Phi=180$ deg, $M=0.5$, $\mathrm{Re}=0.9\times10^6$**

sults were found for a reduced frequency of 0.8. Since the out-of-phase part of the unsteady pressure determines the damping or excitation of the blade motion, it is convenient to define the aerodynamic damping parameter $\Xi=-\mathrm{Im}(Cm)$ with $Cm$ as the time-dependent moment coefficient:

$$Cm(t)=\frac{-\int\frac{\vec{r}}{c}\times\left[p\left(\frac{x}{c},t\right)\frac{dx}{c}\vec{e}_n\right]}{\hat{\alpha}\rho_\infty U_\infty^2} \tag{17}$$

with $\vec{r}$ the vector pointing from the pivot location to an arbitrary point on the surface and $\vec{e}_n$ the unit vector normal to the blade surface. A positive value corresponds to a damped oscillation.

Buffum et al. presented a local stability analysis by plotting $(0.5-x/c)\mathrm{Im}(Cp_{ps}-Cp_{ss})_{1st}$. The numerically predicted local stability in comparison with the experimental data is given in Figs. 7 and 8 for reduced frequencies of 1.2 and 0.8, respectively. For both reduced frequencies the computed local stability was greater than the measured stability between 0 and 40 percent chord length and smaller thereafter. The incorporation of transition for a reduced frequency of 1.2 slightly increased the stability.

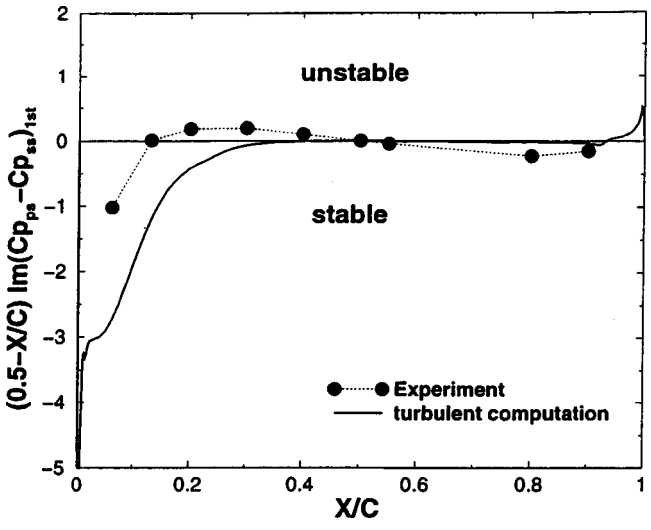


**Fig. 8 Local stability analysis at low incidence, $k=0.8$, $\Phi=180$ deg, $M=0.5$, $\mathrm{Re}=0.9\times10^6$**

Figure 9 shows a counterclockwise variation of the pitching moment during one oscillation cycle thus indicating positive damping. As expected, the aerodynamic damping increased with increased reduced frequency. In this figure the time-dependent development of the moment coefficient is plotted versus the non-dimensional pitching angle $\alpha'=[\alpha(t)-\gamma]/\hat{\alpha}$. As already seen from Fig. 7, including transition slightly increased the damping.

It is of special interest to study the behavior of the separation bubble as a function of the oscillation frequency. Therefore, computations for a reduced frequency of $k=0.2$ were also performed. The bubble length during the blade oscillation was almost 22 percent of chord length, independent of the reduced frequency. For a reduced frequency of 0.2, the largest bubble size occurred shortly after reaching the highest pitching angle. For the reduced frequencies of 0.8 and 1.2 the maximum was reached almost a quarter cycle later. Furthermore, a separation bubble of a maximum size of 3 percent chord length was predicted on the lower surface. The bubble occurred shortly before reaching the lowest pitching angle and vanished completely a quarter cycle later. As expected, a further decrease of the reduced frequency decreased the damping parameter even more. It is also interesting to note that the blade is subjected to a pitching moment fluctuating between positive and negative values for all reduced frequencies.

At low-incidence convergence of the unsteady computations was reached after 6 to 8 cycles using 1000 time steps per cycle and three Newton subiterations for each time step.

**Steady-State High-Incidence Flow.** Contrary to the experimentally determined inflow angle of 70 deg at a pressure ratio of 1.03, the best agreement between the measured and computed pressure distribution was obtained for a pressure ratio of 0.97 resulting in an inflow angle of 67.2 deg; see Fig. 10.

At this angle, the predicted pressure distribution on the lower surface agreed well with the measured data up to 70 percent chord length and was slightly too high thereafter. On the upper surface good agreement was found between the leading edge and 20 percent chord length. Starting at 20 percent chord length the predicted pressure was slightly higher until 45 percent chord length and again between 75 percent chord length and the trailing edge.

A study of the influence of three-dimensional effects due to the formation of corner vortices was performed by varying the $S1$-stream surface thickness of the grid shown in Fig. 1. The two-dimensional numerical results with and without transition shown in Fig. 10 could not be improved by this Quasi-3D computation. Transition onset was found at 0.6 percent chord length on the upper surface while laminar flow to 13 percent chord

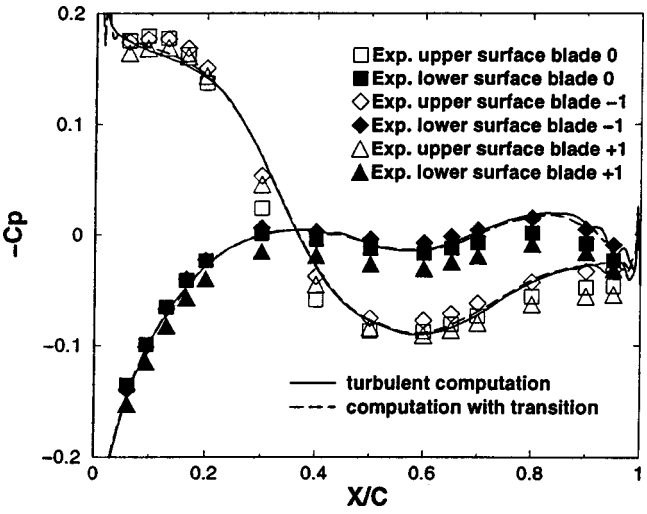


**Fig. 10 Steady-state pressure distribution, $M=0.5$, $\alpha=67.2$ deg, $Re=0.9\times10^6$**

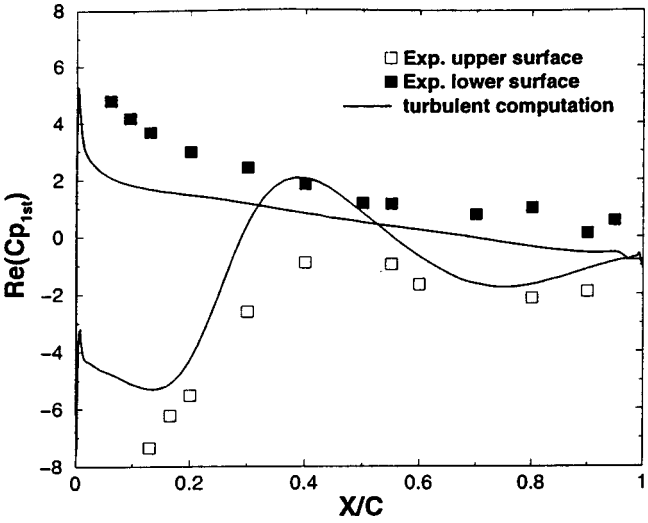


**Fig. 12 Real part of unsteady pressure distribution at high incidence, $k=1.2$, $\Phi=180$ deg, $M=0.5$, $Re=0.9\times10^6$**

length was predicted on the lower surface. The turbulent boundary layer was re-laminarized at the trailing edge. Including transition improved the predicted pressure distribution on the upper surface between the leading edge and 20 percent chord length. In Fig. 11 the steady-state Mach number contours show the separated flow region on the upper surface. A bubble of almost 50 percent chord length was found that was 10 percent longer than the measured bubble.

**Flutter at High Incidence.** Measurements for reduced frequencies of 0.4, 0.8, and 1.2 were taken at high incidence. In Figs. 12 and 13 the computed real and imaginary parts of the first harmonic unsteady pressure coefficient at a reduced frequency of 1.2 are compared with the experimental results. Although the measured trend of the real part, especially on the upper surface, was predicted by the computation, the agreement is less accurate than for the low incidence case; see Fig. 5. However, in contrast to the unsteady low incidence computations, the predicted imaginary part at high incidence is in better agreement with the experimental results than the real part. A similar behavior was found for the reduced frequencies of 0.4 and 0.8. The overall agreement became slightly worse with decreasing reduced frequency. The opposite behavior was found for the low-incidence computations.

In Fig. 14 snapshots of the unsteady Mach number contours at a reduced frequency of 1.2 are shown. The snapshots were taken at four different times during one cycle *T*. Here the development of the separation bubble from a small bubble to a bubble extending to 64 percent chord length can be seen.

A comparison of the low- and high-incidence measurements of the local stability, Figs. 7, 8, 15, 16, 17, shows that the leading edge region makes a decisive contribution to the total stability. In the low-incidence case the leading edge contributes positive damping, whereas in the high-incidence case the flow separation near the leading edge on the upper surface causes a destabilizing pitching moment. As seen in Figs. 15, 16, 17, the computations fail to capture this destabilizing leading edge moment, but the local moment contribution from about 15 percent chord to the

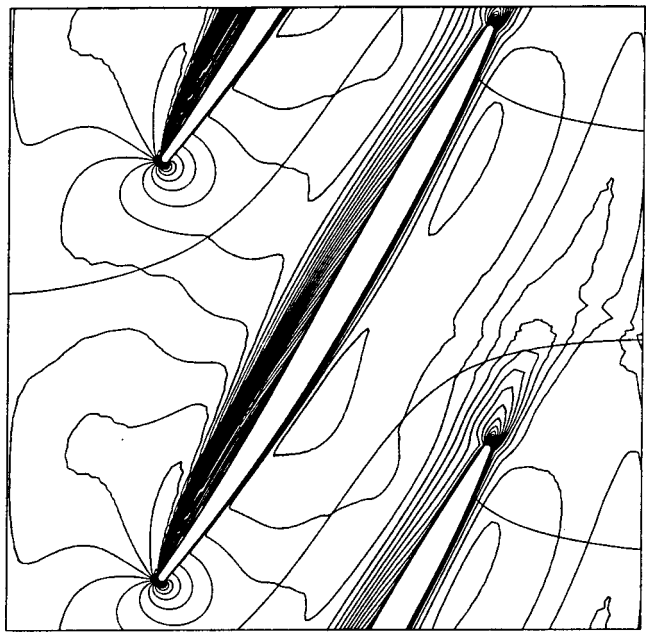

**Fig. 11 Steady-state Mach number contours, $M=0.5$, $\alpha=67.2$ deg, $Re=0.9\times10^6$**

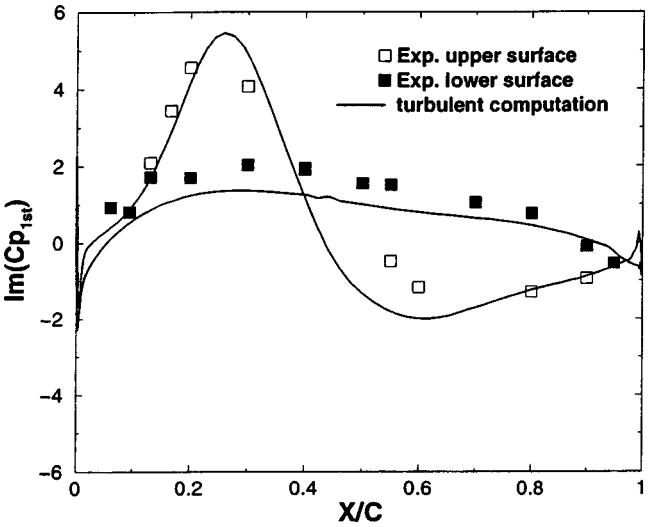


**Fig. 13 Imaginary part of unsteady pressure distribution at high incidence, $k=1.2$, $\Phi=180$ deg, $M=0.5$, $Re=0.9\times10^6$**

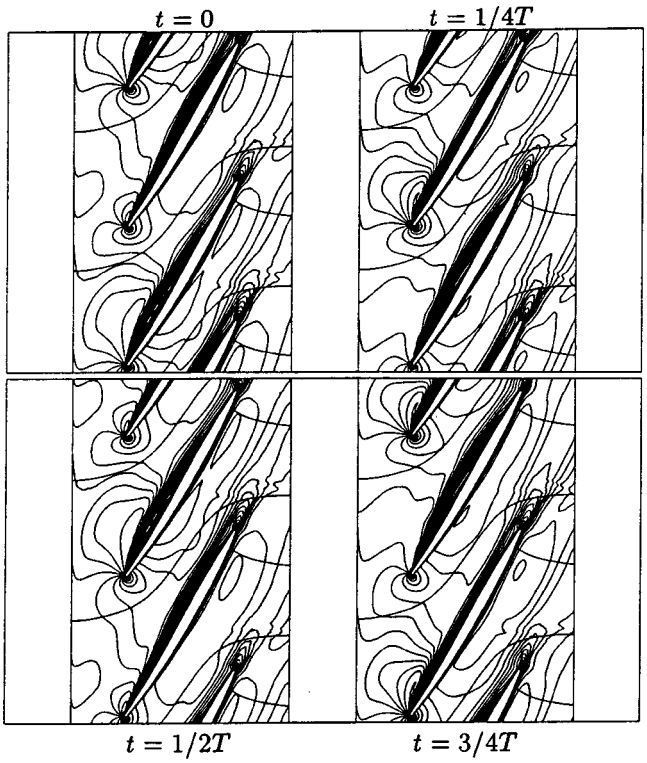


**Fig. 14 Predicted unsteady Mach number contours at high incidence, $k=1.2$, $\Phi=180$ deg, $M=0.5$, Re$=0.9\times10^6$**

trailing edge are predicted quite well for $k=1.2$, while significant differences are apparent up to midchord for the $k=0.8$ and $k=0.4$ cases. A separation bubble is found to exist on the upper surface during the complete oscillation cycle. At $t=0.14T$ the bubble reaches its smallest length of 34 percent chord length, which is 16 percent less than in the steady-state solution. The largest bubble is seen at $t=0.9T$, where it reaches a length of 65 percent chord. On the lower surface the flow remained attached during the complete oscillation cycle.

The pitching moment hysteresis loops and the damping parameter in dependency of the reduced frequency are given in Fig. 18.

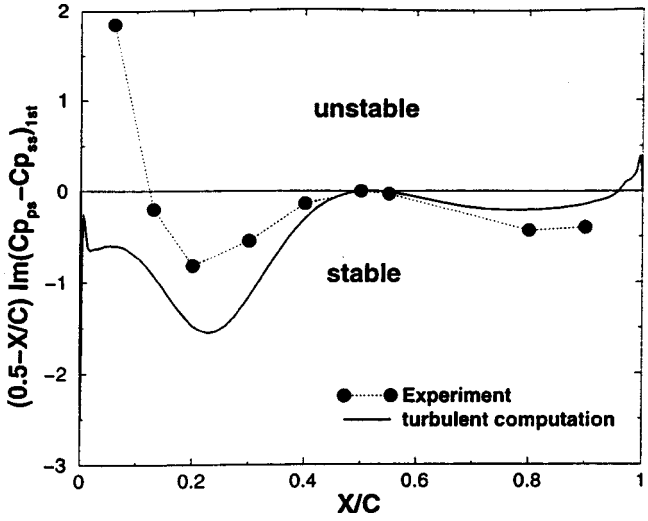


**Fig. 16 Local stability analysis at high incidence, $k=0.8$, $\Phi=180$ deg, $M=0.5$, Re$=0.9\times10^6$**

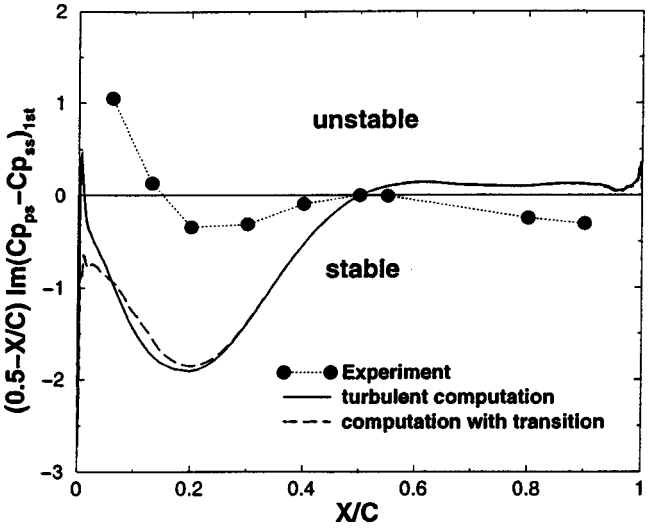


**Fig. 17 Local stability analysis at high incidence, $k=0.4$, $\Phi=180$ deg, $M=0.5$, Re$=0.9\times10^6$**

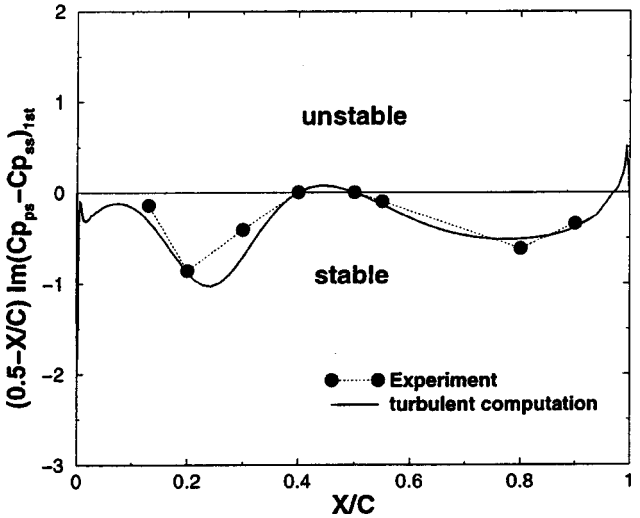


**Fig. 15 Local stability analysis at high incidence, $k=1.2$, $\Phi=180$ deg, $M=0.5$, Re$=0.9\times10^6$**

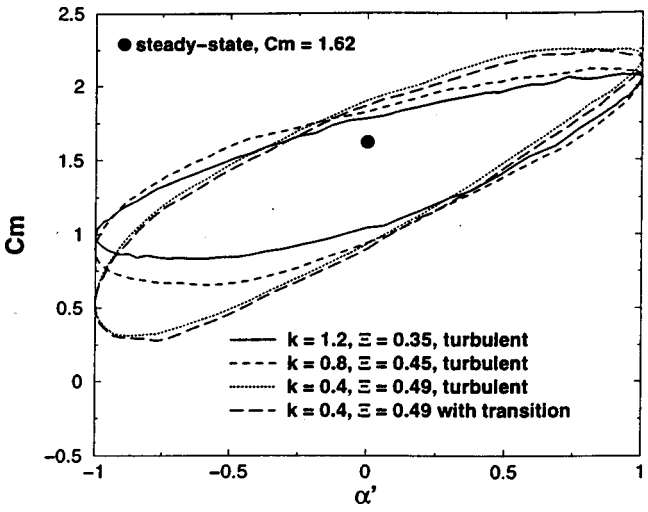


**Fig. 18 Predicted unsteady aerodynamic moment coefficient at high incidence, $\Phi=180$ deg, $M=0.5$, Re$=0.9\times10^6$**

The almost elliptical shape of the hysteresis loops indicate a linear response of the flow field to the prescribed motion. Furthermore, in contrast to the low-incidence case, the pitching moment is seen to be positive for all reduced frequencies.

Convergence of the computations for the different high-incidence cases was obtained after 8 to 12 cycles. As for the low-incidence case, 1000 time steps per cycle in combination with three Newton subiterations for each time step were used. All computations were performed on SGI Octane 250 MHz, R10000 workstations, and Pentium II-400 Linux PCs.

## Concluding Remarks

At low incidence the steady and oscillatory flow cases showed encouraging agreement with the experiment. As expected, the computed aerodynamic damping increased with increasing oscillation frequency. These results are consistent with the time-linearized Navier–Stokes computations of Clark and Hall [2].

On the other hand, at high incidence the numerical model failed to predict the negative damping close to the leading edge although the steady-state solution was in good agreement with the measured data.

This failure suggests to explore the use of more sophisticated transition and turbulence modeling. Such models were already incorporated for the prediction of dynamic stall on single airfoils and led to significantly improved agreement with the available experimental data, as summarized by Ekaterinaris and Platzer [9]. Therefore, it is planned to apply these models in the next series of computations for the Buffum cascade.

## Acknowledgments

The first author gratefully acknowledges the support of the Deutsche Forschungsgemeinschaft (DFG) and the Naval Postgraduate School.

## References

[1] AGARDograh No. 298, 1987, AGARD Manual on Aeroelasticity in Axial-Flow Turbomachines.
[2] Clark, W. S., and Hall, K. C., 2000, ''A Time-Linearized Navier–Stokes Analysis of Stall Flutter,'' ASME J. Turbomach., **122**, pp. 467–476.
[3] Hall, K. C., and Crawley, E. F., 1993, ''Calculation of Unsteady Flows in Turbomachinery Using the Linearized Euler Equations,'' AIAA J., **27**, pp. 777–787.
[4] Kahl, G., and Klose, A., 1993, ''Computation of Time Linearized Transonic Flow in Oscillating Cascades,'' ASME Paper No. 93-GT-269.
[5] Montgomery, M. D., and Verdon, J. M., 1995, ''A Linearized Unsteady Euler Analysis for Turbomachinery Blade Rows Using an Implicit Wave-Split Scheme,'' *Proc. 7th Int. Symp. on Unsteady Aerodynamics and Aeroelasticity of Turbomachines*, Elsevier Science b.v. Amsterdam.
[6] Baldwin, B. S., and Lomax, H., 1978, ''Thin Layer Approximation and Algebraic Model for Separated Turbulent Flow,'' AIAA Paper No. 78–257.
[7] Baldwin, B. S., and Barth, T. J., 1990, ''A One-Equation Turbulence Transport Model for High Reynolds Number Wall-Bounded Flows,'' NASA TM 102847.
[8] Spalart, P. R., and Allmaras, S. R., 1992, ''A One-Equation Turbulence Model for Aerodynamic Flows,'' AIAA Paper No. 92-0439.
[9] Ekaterinaris, J. A., and Platzer, M. F., 1997, ''Computational Prediction of the Airfoil Dynamic Stall,'' Prog. Aerosp. Sci., **33**, pp. 759–846.
[10] Sanz, W., and Platzer, M. F., 1998, ''On the Navier–Stokes Calculation of Separation Bubbles With a New Transition Model,'' ASME J. Turbomach., **120**, pp. 36–42.
[11] Weber, S., and Platzer M. F., 1999, ''Steady and Dynamic Stall Analysis of the NLR 7301 Airfoil,'' ASME Paper No. 99-GT-21.
[12] Weber, S., Jones, K. D., Ekaterinaris, J. A., and Platzer, M. F., 1999, ''Transonic Flutter Computations for a 2D Supercritical Wing,'' AIAA Paper No. 99-0798.
[13] Eulitz, F., 1999, ''Unsteady Turbomachinery: Numerical Simulation and Modelling,'' *Proc. ODAS 99*, ONERA-DLR Aerospace Symposium.
[14] Bakhle, M. A., Srivastava, R., Stefko, G. L., and Janus, J. M., 1996, ''Development of an Aeroelastic Code Based on an Euler/Navier–Stokes-Aerodynamic Solver,'' ASME Paper No. 96-GT-311.
[15] Chew, J. W., Marshall, J. G., Vahdati, M., and Imegrum, M., 1998, ''Part-Speed Flutter Analysis of a Wide-Chord Fan Blade,'' *Proc. 8th Int. Symp. on Unsteady Aerodynamics and Aeroelasticity of Turbomachines*, Stockholm, Kluwer Academic Publishers.
[16] He, L., 1993, ''New Two Grid Acceleration Method for Unsteady Navier–Stokes Calculations,'' J. Propul. Power, **9**, pp. 272.
[17] Eguchi, T., and Wiedermann, A., 1995, ''Numerical Analysis of Unstalled and Stalled Flutter Using a Navier–Stokes-Code with Deforming Meshes,'' *Proc. 7th Int. Symp. on Unsteady Aerodynamics and Aeroelasticity of Turbomachines*, Elsevier Science b.v. Amsterdam.
[18] Abhari, R. S., and Giles, M., 1997, ''A Navier–Stokes Analysis of Airfoils in Oscillating Transonic Cascades for the Prediction of Aerodynamic Damping,'' ASME J. Turbomach., **119**, pp. 77–84.
[19] Grüber, B., and Carstens, V., 1998, ''Computation of the Unsteady Transonic Flow in Harmonically Oscillating Turbine Cascades Taking Into Account Viscous Effects,'' ASME J. Turbomach., **120**, pp. 104–111.
[20] Weber, S., Benetschik, H., Peitsch, D., and Gallus, H. E., 1997, ''A Numerical Approach to Unstalled and Stalled Flutter Phenomena in Turbomachinery Cascades,'' ASME Paper No. 97-GT-102.
[21] Weber, S., Gallus, H. E., and Peitsch, D., 1998, ''Numerical Solution of the Navier–Stokes Equations for Unsteady Unstalled and Stalled Flow in Turbomachinery Cascades With Oscillating Blades,'' *Proc. 8th Int. Symp. on Unsteady Aerodynamics and Aeroelasticity of Turbomachines*, Stockholm, Kluwer Academic Publishers.
[22] Kato, D., Outa, E., and Chiba, K., 1998, ''On Sub-Cell Structure of Deep Rotating Stall in an Axial Compressor,'' *Proc. 8th Int. Symp. on Unsteady Aerodynamics and Aeroelasticity of Turbomachines*, Stockholm, Kluwer Academic Publishers.
[23] Tuncer, I. H., Weber, S., and Sanz, W., 1999, ''Investigation of Periodic Boundary Conditions in Multipassage Cascade Flows Using Overset Grids,'' ASME J. Turbomach., **121**, pp. 341–347.
[24] Carstens, V., and Schmitt, S., 1999, ''Comparison of Theoretical and Experimental Data for an Oscillating Transonic Compressor Cascade,'' ASME Paper No. 99-GT-408.
[25] Fourmaux, A., 1999, ''Blade-Row Interaction in a Transonic Turbine,'' *Proc. ODAS 99*, ONERA-DLR Aerospace Symposium.
[26] Lin, J.-S., and Murthy, D. V., 1999, ''Unsteady Aerodynamic Analysis of an Oscillating Cascade at Large Incidence,'' ASME Paper No. 99-GT-22.
[27] Buffum, D. H., Capece, V. R., and El-Aini, Y. M., 1998, ''Oscillating Cascade Aerodynamics at Large Mean Incidence,'' ASME J. Turbomach., **120**, pp. 122–130.
[28] Benetschik, H., 1991, ''Numerische Berechnung der Trans- und Überschall-Strömung in Turbomaschinen mit Hilfe eines impliziten Relaxationsverfahrens,'' Doctorthesis, RWTH Aachen, Germany.
[29] Roe, P. L., 1981, ''Approximative Riemann Solvers, Parameter Vectors and Difference Schemes,'' J. Comput. Phys., **43**, pp. 357–372.
[30] Harten, A., 1983, ''High Resolution Schemes for Hyperbolic Systems of Conservation Laws,'' J. Comput. Phys., **49**, pp. 357–393.
[31] van Leer, B., 1979, ''Towards the Ultimative Conservative Difference Scheme V, A Second Order Sequel to Godunov's Method,'' J. Propul. Power, **32**, pp. 101–136.
[32] Rai, M. M., and Chakravarthy, S. R., 1986, ''An Implicit Form of the Osher Upwind Scheme,'' AIAA J., **24**, No. 5, pp. 735–743.
[33] Chakravarthy, S. R., 1983, ''Euler Equations—Implicit Schemes and Boundary Conditions,'' AIAA J., **21**, No. 5, pp. 699–705.
[34] Erdos, J. I., Alzner, E., and McNally, W., 1977, ''Numerical Solution of Periodic Transonic Flow Through a Fan Stage,'' AIAA J., **15**, pp. 1559–1568.
[35] Peitsch, D., Gallus, H. E., and Weber, S., 1995, ''Computation of Unsteady Transonic 3D-Flow in Turbomachine Bladings,'' *Proc. 7th Int. Symp. on Unsteady Aerodynamics and Aeroelasticity of Turbomachines*, Elsevier Science b.v. Amsterdam.